Int. J. Environ. Sci. Technol. (2016) 13:1525–1540
DOI 10.1007/s13762-016-0995-2

ORIGINAL PAPER

Unsteady flow over offshore wind turbine airfoils and aerodynamic loads with computational fluid dynamic simulations

M. Abbaspour[1] · A. R. Radmanesh[1] · M. R. Soltani[2]

Received: 21 August 2015 / Revised: 31 March 2016 / Accepted: 12 April 2016 / Published online: 4 May 2016

Abstract The first notable megawatt class wind turbine, which was the pioneer of improvement in the blade performance in large wind turbines, appeared in Vermont. Nowadays, modern wind turbines are using blades with multi-airfoils at different sections. In this study, in order to indicate the best airfoil profile for the optimum performance in different sections of a blade, five popular airfoils, including S8xx, FFA and AH series, were studied. On the large-scale profile, shear stress transport K–ω model was applied for the simulation of horizontal axis wind turbines for different wind speeds. The aerodynamic simulation was accomplished using computational fluid dynamic method, which in turn is based on the finite volume method, and semi-implicit method for pressure-linked equations algorithm is used for pressure–velocity coupling. The governing equations applied in this simulation are the unsteady Reynolds-averaged Navier–Stokes equations. The aerodynamic coefficients of lift and drag were calculated at different angle of attacks and different wind speeds. The results were validated by EPPLER code, XFOIL and experimental data of the US National Renewable Energy Laboratory. The results showed that S818 profile is the best profile in terms of gaining the highest lift coefficient with the lowest angle of attack at the root of the blades. The findings also indicated that the selected model can predict the exact geometry with a high precision.

✉ A. R. Radmanesh
radmanesh@tic.sharif.edu

[1] Center of Excellence in Energy Conversion and School of Mechanical Engineering, Sharif University of Technology, Tehran 11155-9567, Iran

[2] Department of Aerospace Engineering, Sharif University of Technology, Tehran 1458889694, Iran

Keywords Wind turbine · Computational fluid dynamic · Unsteady aerodynamic simulation · National Renewable Energy Laboratory

Introduction

The first wind turbines were used in Persia (present-day Iran) in the seventh century. They were vertical axis windmills which had long vertical drive shafts with rectangular blades. However, the first notable contemporary research was conducted in 1941, when the first megawatt class wind turbine was synchronized to a utility grid in Vermont, in 1941. It was concluded that to improve the blade performance in large wind turbines, their aerodynamics must be enhanced. For many years, researchers have studied the performance of large wind turbines in order to increase their power. The new generation as well as large scale wind turbines with the approximate power output of 1.5–10 MW have the optimum performance at the speed range of 10–15 m/s. The best power coefficient depends on the design of the rotor blade (i.e., for this study, a comparison was conducted among several main groups of airfoil for large-scale wind turbines). The modern horizontal axis wind turbine (HAWT) blades are designed using combinations of airfoil families (Hansen and Butterfield 1993) where the blade tip is designed using a thin airfoil for high lift to drag ratio and the root utilizes a thick version of the same airfoil for structural support. Generally, in the 1970s and early 1980s, wind turbine designers felt that minor differences in airfoil performance characteristics were far less important than optimizing blade twist. Sayed and Kandil worked on a 2D model by computational fluid dynamic Reynolds-averaged Navier–Stokes (CFD-RANS) for the S series wind turbine blade profiles at low Reynolds numbers. Moreover, a two-dimensional computation utilizing the CFD-RANS equations have been implemented at low Reynolds numbers for the wind turbine blade profiles of S809 and S826 by Sayed et al. Furthermore, Mohammad and Kandil worked on an aerodynamic analysis of different wind turbine profiles using RANS at different angle of attacks (AOAs) for each blade profile (Sayed et al. 2012). Le Pape and Lecanu used ONERA's code Elsa, a structured multi-block solver, to model the NREL Unsteady Aerodynamics Experiment in an upwind zero yaw configuration. Finally, at the end of 1989, a 300-kW wind turbine with a 30 m rotor diameter was considered too large, whereas by early 2004, 4- to 5-MW wind turbines became available (Ackermann 2005). Additionally, aerodynamic design and performance attempts to simulate laminar flow on a blade were performed by Bumsuk.

This article focused on the load and dynamic stability of a wind power generation system (Kim et al. 2011). Farrugia worked on the aerodynamic performance of a model of offshore floating wind turbine, specifically on the effects of wave-induced motions on the rotor aerodynamic variables (Farrugia et al. 2014). On the other hand, dynamics modeling for the offshore floating vertical axis wind turbine models were done by Borg. Highlighting the fundamental theory while providing a general review of the latest works, and for authority in this area, providing comprehensive researches (Borg et al. 2014). Previously, Cheng had investigated of a high-performance offshore wind turbine. The present investigation studied aerodynamic analysis, and its results can form a basis for evaluating aerodynamic performance of large-scale offshore wind turbine rotors (Cheng et al. 2010). In this field, outstanding research on the implementations of these systems has been done by Manwell. In this research, the focus was on a comparison between onshore and offshore wind turbines, specifically considering offshore wind energy technology trends, challenges and risks (Manwell 2012).

The literature clearly shows that a wide range of researchers have focused on high speeds and there is no comprehensive research on the low-speed range specifically using unsteady Reynolds-averaged Navier–Stokes (URANS) equations (Sayed and Morgan 2011) on high-capacity wind turbine airfoils. In line with this objective, the main goal of this study was to investigate the main types of wind turbines and to develop 2D analysis of HAWT by CFD methods.

The designs encompass a wide range of AOA and velocities to increase the efficiency of the wind turbine for maximum power. In this study, the power is determined by analyzing the flow around a section of the blade. The wind turbine blade profiles are selected from the profiles developed by the National Renewable Energy Laboratory (NREL) and AH and FFA (Björk 1996).

On the point of other researches, the effect of accelerated flow over moving airfoil in unsteady aerodynamics conditions was done by Esfahani. This model accurately predicts the unsteady aerodynamic of S809, and numerical models have been utilized to estimate the dynamic stall and predict the aerodynamic behavior (Karbasian et al. 2014). A new special airfoil shape (DU93-W-210) has been developed and optimized for wind turbine using genetic algorithm (GA). This article has been written by Yixiong Liu. The optimum airfoil is obtained with CFD method by solving the RANS equations for improving the performance and efficiency of the optimization algorithm (Liu et al. 2015). The experimental analysis of onshore wind turbine airfoil NACA2415 was done by Driss. This investigation has been developed for experimental stimulation to estimate the velocity and torque variation for different Reynolds numbers and AOAs. All the numerical results were validated with CFD method (Driss et al. 2015).

In recent years, many researchers have done work to predict the behavior of the flow with active stall control. Three airfoil families with respect to adaptive pitch control for variable speed were developed, Risø-A1, Risø-P and Risø-B1, by Fuglsang. The obtained numerical results have been adapted with CFD code Ellipsys2D for prediction of airfoil pressure coefficient distribution. Different techniques were studied as well as ways to predictions of airfoil roughness sensitivity (Fuglsang and Bak 2004). A new investigation for unsteady aerodynamic large scale wind turbine has been made by Radmanesh. This article emphasizes the importance of including the effect of unsteady aerodynamics conditions and meshes quality on the role of high fidelity in stall and post-stall condition (Radmanesh 2014, 2015a, b).

Design approach

For this study, three main groups of airfoil geometry were used. The following airfoil series will be discussed:

1. FFA-W-xxx, Flygtekniska Forsoks Anstalten (The Aeronautical Research Institute of Sweden) (van Rooij and Timmer 2003).
2. S8xx design from D. Somers (xx is serial number) (van Rooij and Timmer 2003).
3. AH xx-W-xxx, D. Althaus from Institute for Aerodynamics and Gas dynamics of the University of Stuttgart, Germany (van Rooij and Timmer 2003).

By comparing different airfoils, aerodynamic coefficients for each profile are determined at different AOAs (Sayed and Morgan 2011). Air flow over an airfoil

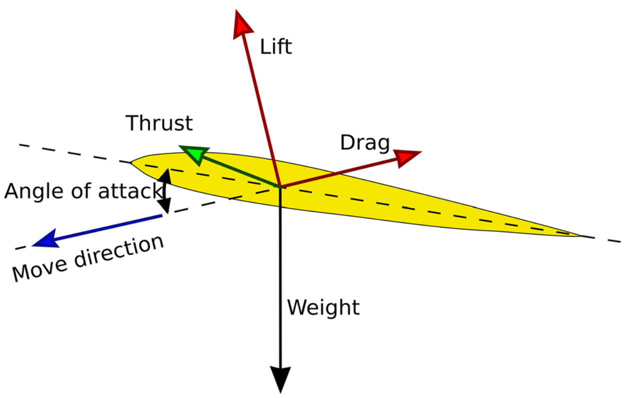

Fig. 1 Forces on an airfoil section

produces a distribution of forces over the airfoil surface. The flow velocity over airfoil increases over the convex surface resulting in lower average pressure on the suction side of the airfoil compared with the concave or pressure side of the airfoil. As shown in Fig. 1, the resultant of all of these pressure and friction forces are usually resolved into two forces and a moment that act along the chord at a distance of c/4 from the leading edge.

Lift force perpendicular to the direction of the oncoming airflow is a consequence of the unequal pressures on the upper and lower airfoil surfaces.

$$C_{\mathrm{L}} = \frac{L}{\frac{1}{2}\rho V^2 A} = \frac{\text{Lift Force}}{\text{Dynamic Force}} \tag{1}$$

Drag force parallel to the direction of the oncoming airflow is due to both the viscous friction forces at the surface of the airfoil and the two unequal pressures on the airfoil surfaces facing toward and away from the incoming flow (Manwell et al. 2009).

$$C_{\mathrm{D}} = \frac{D}{\frac{1}{2}\rho V^2 A} = \frac{\text{Drag Force}}{\text{Dynamic Force}} \tag{2}$$

The most important non-dimensional parameter for defining the characteristics of fluid flow conditions is the Reynolds number. The Reynolds number (*Re*) is defined by (Manwell et al. 2009):

$$Re = \frac{UX}{\upsilon} = \frac{\rho UX}{\mu} = \frac{\text{Inertial Force}}{\text{Viscos Force}} \tag{3}$$

Other dimensionless coefficients that are important for the analysis and design of wind turbines include the pressure coefficient and the sliding ratio (Manwell et al. 2009):

$$C_{\mathrm{p}} = \frac{P - P_{\infty}}{\frac{1}{2}\rho U^2} = \frac{\text{Static Pressure}}{\text{Dynamic Pressure}} \tag{4}$$

$$\varepsilon = \frac{C_{\mathrm{L}}}{C_{\mathrm{D}}} = \frac{L}{D} \tag{5}$$

Materials and methods

The aerodynamic simulations of unsteady flow at low speed over 2D wind turbine blade profiles are solved by using CFD technique based on the finite volume method. A finite volume solver based on forms of unsteady Reynolds-averaged Navier–Stokes (URANS) equations was used in the present study. The governing equations used in the simulation are the URANS equations (Gatski and Bonnet 2009; Hirsch 1990; Wilcox 2006). The new generations of horizontal axis wind turbines (HAWTs) are using thin airfoils for the high sliding ratio, and root region is designed using a thick airfoils (Sayed et al. 2012). Airfoils have a greater thickness resulting in greater blade stiffness and tower clearance. The turbulence model of shear stress transport (SST K–ω) is available (Menter 1994; Wilcox 2006) and is known to accurately predict the size of a vortex and the location of the separation point caused by adverse pressure gradient. Thus, the SST model is one of the best turbulence models for this study. The governing equation is integrated in a structured mesh with approximately 35,000 elements. The computational domain dependency tests were applied to optimize the domain size and find the trustable optimum domain size for reducing the number of meshes and obtain the optimum grid size for minimum grid (Mark and Dimitri 2009). Consequently, the platform model detailed and optimized the computational domain in order to get an optimum domain size. Independent solution and the high-resolution domain size are represented in Fig. 2. Moreover, the optimized domain based on the number of grids and the grid shape on this simulation is shown in Fig. 2.

In order to reduce the numerical solution errors and the fast convergence for other components, the upwind scheme method has been chosen. Velocity gradient occurs near the wall; therefore, it needs a boundary layer and elements with high aspect ratio. The boundary condition around the airfoil has been set to no-slip solid wall boundary. In this study, all five cases are solved at multiple wind speeds that make their results comparable with each other and the numbers of the points are increased for more accuracy. In order to optimize stopping criteria, the convergence in different process levels are evaluated when the number of iterations and AOA are different. In addition, iterative convergence error depends on the stopping criteria, and by increasing AOA, the behavior of the convergence is changed and, in some cases, leads to divergence. In addition, having a near-wall modeling approach will possess the resolution of the standard two-layer approach for fine near-wall meshes and, simultaneously, will not significantly reduce precision for wall-function meshes. It is worth mentioning that ANSYS FLUENT software provides us with the two-layer model with increased wall functions (ANSYS 2014).

The blade profiles used in the simulation are represented in Fig. 3. The simulation included a range of angle of attacks (AOAs) from −5° to 20°, because it is a normal condition of the wind turbine to obtain a maximum efficiency. The objective of the simulation was to find the optimum operating AOA that produces the maximum power from the wind turbine blades based on the maximum lift to drag forces (Langtry et al. 2006).

Turbulence modeling relation

Menter's SST turbulence model is a widely used and robust two-equation eddy-viscosity turbulence model used in CFD. The K–ω turbulence model and K–ε turbulence model is combined such that the K–ω is employed in the internal area of the boundary layer and changes to the K–ε in the free shear flow (Menter 1994).

All forms of the model appointed in this paper are linear eddy-viscosity models. Linear models use the Boussinesq assumption:

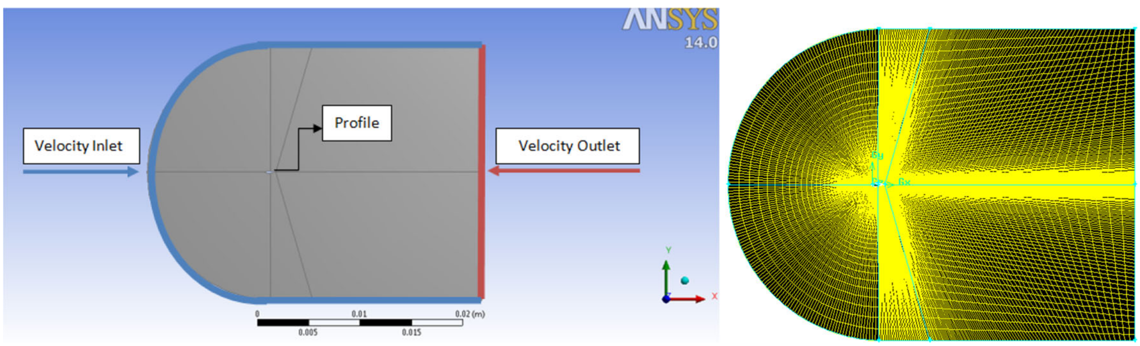

Fig. 2 Computational domain and final mesh

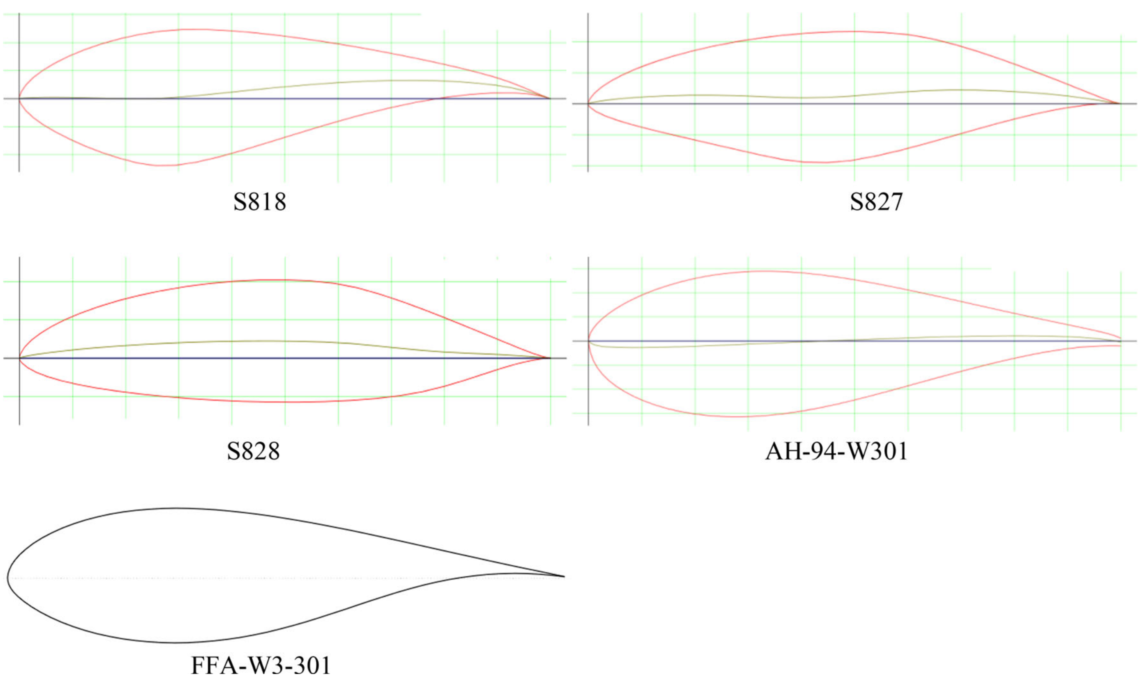

Fig. 3 Airfoil shapes

$$\tau_{ij} = 2\mu_t\left(S_{ij} + \frac{1}{3}\frac{\partial u_k}{\partial x_k}\delta_{ij}\right) - \frac{2}{3}\rho k\delta_{ij} \tag{6}$$

"Standard" Menter SST two-equation model (SST) (Menter 1994)

$$\frac{\partial(\rho k)}{\partial t} + \frac{\partial(\rho u_j k)}{\partial x_j} = P - \beta^*\rho\omega k + \frac{\partial}{\partial x_j}\left[(\mu + \sigma_k\mu_t)\frac{\partial k}{\partial x_j}\right] \tag{7}$$

$$\frac{\partial(\rho\omega)}{\partial t} + \frac{\partial(\rho u_j\omega)}{\partial x_j} = \frac{\gamma}{\upsilon_t}P - \beta^*\rho\omega^2 + \frac{\partial}{\partial x_j}\left[(\mu + \sigma_\omega\mu_t)\frac{\partial\omega}{\partial x_j}\right] + 2(1 - F_1)\frac{\rho\sigma_{\omega 2}}{\omega}\frac{\partial k}{\partial x_j}\frac{\partial\omega}{\partial x_j} \tag{8}$$

In this paper, the Lagrangian derivative was used

$$P = \tau_{ij}\frac{\partial u_j}{\partial x_j} \tag{9}$$

$$\tau_{ij} = \mu_t\left(S_{ij} + \frac{2}{3}\frac{\partial u_k}{\partial x_k}\delta_{ij}\right) - \frac{2}{3}\rho k\delta_{ij} \tag{10}$$

$$S_{ij} = \frac{1}{2}\left(\frac{\partial u_i}{\partial x_j} + \frac{\partial u_j}{\partial x_i}\right) \tag{11}$$

And the turbulent eddy viscosity is computed from:

$$\mu_t = \frac{\rho a_1 k}{\max(a_1\omega, \Omega F_1)} \tag{12}$$

Results and discussion

The performance of the S818, S827, S828, FFA-W3-301 and AH-94-W301 at different wind speeds and the comparison of the measured C_L and C_D curves compared with XFOIL and EPPLER code calculations (Gonzalez and Munduate 2007; Tangler 1982) are demonstrated in Fig. 4. As shown in Fig. 4, lift coefficient airfoils are conducted for the whole range of wind speeds and AOAs. In summary, the measurement results illustrate good agreement between measurements and the XFOIL and EPPLER calculations in low AOA. At higher AOA in the stall and in the post-stall region, calculations have overestimated the maximum C_L for S818 and FFA-W3-301. For this modeling, S818, FFA-W3-301 and AH-W3-301 have thick airfoils and the rest have thin airfoils, since the first group consists of the root airfoils and the second group contains the primary and tip airfoils. As shown in Fig. 5, as the sliding ratio increases, greater maximum power is obtained at the same range of AOA at different wind speeds (Langtry et al. 2006). Results indicate the best operating condition for each profile with respect to the variation in AOA and wind speed. For the FFA-W3-301and S818 profiles, which represented in Fig. 5a, b, the best operating AOA is at 5° and 10°, because their maximum thickness occurs between X/C = 40–50 % of the chord (locations of the maximum relative thickness). The S818 airfoil has a maximum camber of 3.3 % at 74.2 % chord (0.742 chords) from the leading edge with a maximum thickness of 24 % at 30.9 % chord (Buhl 2012). As a general rule to obtain good stall characteristics, effects of relative thickness on airfoil performance should be considered, because the thickness of the airfoil has a major impact on how separation develops on the airfoil. Moreover, in thick airfoil the separation appears in trailing edge and move forward by increasing AOA (Ma et al. 2015). Meanwhile, according to above information in order to obtain the highest possible airfoil performance, the location of the maximum relative thickness should be closer to the trailing edge, and consequently, the value of maximum relative thickness should be the minimum possible value (Gudmundsson 2014). The other S827 and S828 profiles operate best at AOAs between 0° and 5°, because the maximum thickness occurs between X/C = 20–40 % of the chord (Yelmule and EswaraRao Anjuri 2013).

The lift coefficient increased for all of the profiles when the wind speed was amplified. Also, the lift coefficient increased with the increase in the AOA between 5° and 15° and then began to decrease in AOAs greater than 15° at constant wind speed. Comparisons of the theoretical and experimental results, as well as the EPPLER Airfoil Design and Analysis Code, generally showed a good agreement with the exception of maximum lift, which was significantly underestimated (Gonzalez and Munduate 2007; Somers 2005). The lift coefficient curves provided in Fig. 4f are for 3.3 % camber at 0.742 chords. Compared to performance at higher Reynolds numbers (V = 30 m/s, $Re = 1.4 \times 10^5$), the study demonstrates in post-stall region at the AOA = 15, where the maximum error occurs, and the maximum deviation between EPPLER code at $Re = 1.44 \times 10^5$ and ANSYS commercial code at V = 30 m/s is approximately less than ±11.9 %. However, both analyses indicate similar reductions in the lift curve slope and equivalent increases in drag, and after AOA = 17, the maximum deviation is reduced, approximately less than ±9.6 %. Besides, results fairly match the XFOIL and EPPLER calculations in low AOA. It should be noted that the experimental results have done by the Aeronautical Research Institute of Sweden and endorsed by US National Renewable Energy Laboratory (NREL). NREL's R&D experimental result is available just for FFA-W3-301 (Bjorck 1990).

The velocity and pressure distribution around the S818, S827 and S828 airfoils are shown in Fig. 6a–l. They indicate that the airfoil has two major components, which includes the upper surface as a convex wall and the lower surface as a concave wall that are connected at leading and trailing edges. The velocity on the upper surface is higher

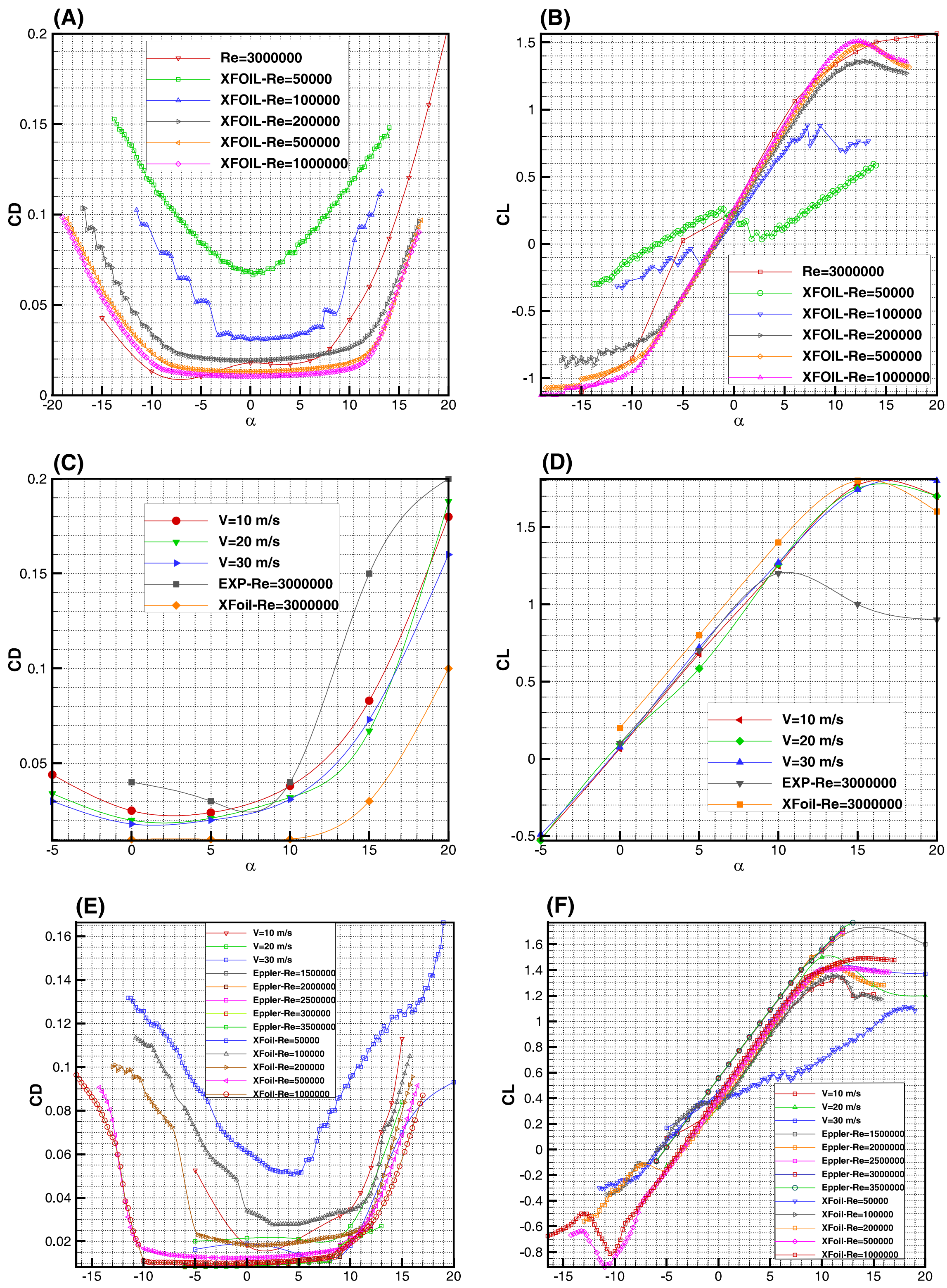

Fig. 4 Lift and drag performance. **a** The drag performance for AH 94-W-301, **b** the lift performance for AH 94-W-301, **c** the drag performance for FFA-W3-301, **d** the lift performance for FFA-W3-301, **e** the drag performance for S818, **f** the lift performance for S818, **g** the drag performance for S827, **h** the lift performance for S827, **i** the drag performance for S828 and **j** the lift performance for S828

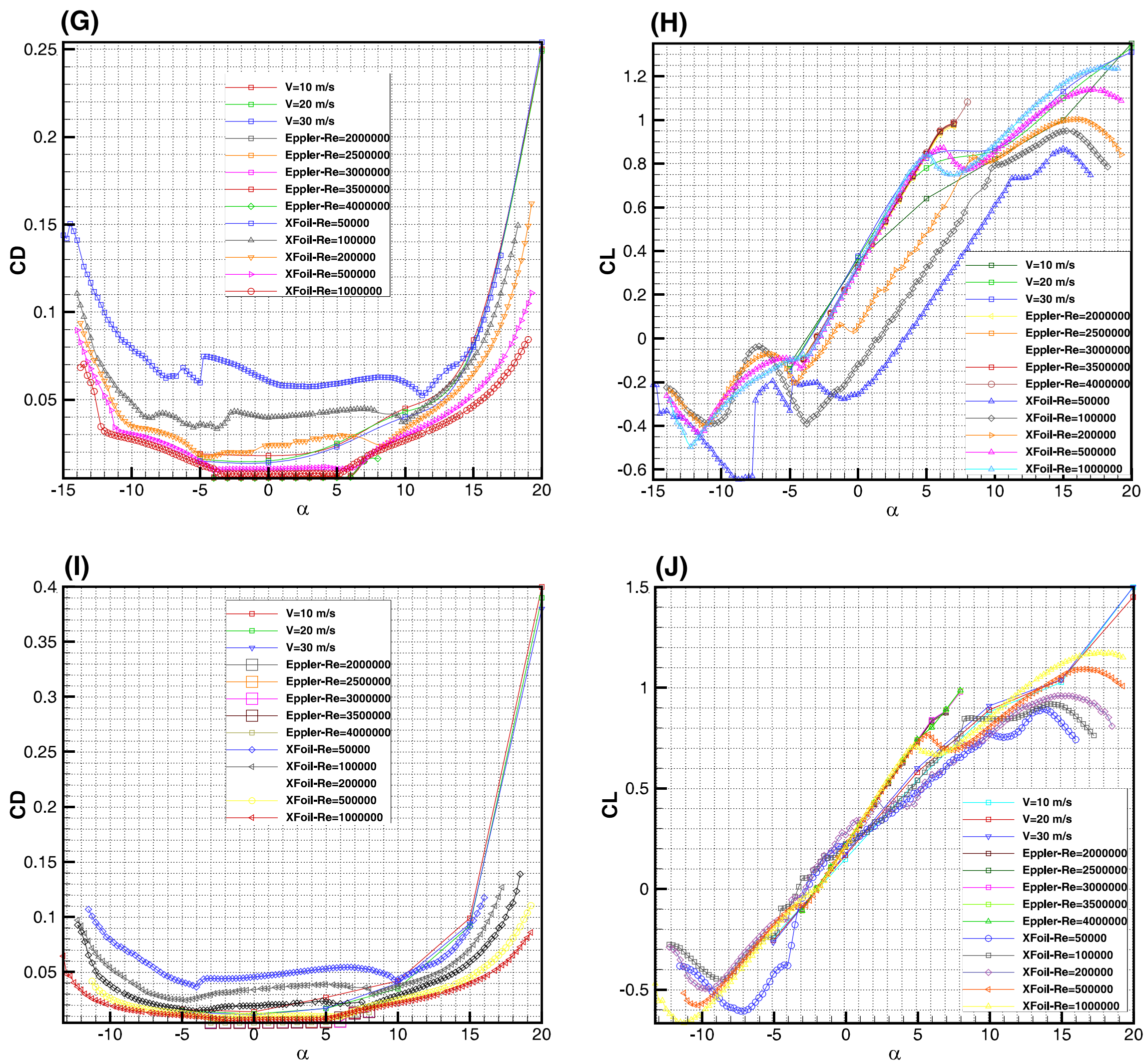

Fig. 4 continued

than velocity on the lower surface; according to the Bernoulli's equation, the pressure on the lower surface (under the leading edge) of the airfoil is higher than the pressure over the upper surface (Slooff 2015). Moreover, the pressure on the lower surface of the airfoil close to the trailing edge depends on form and thickness of the airfoil. As shown in Fig. 6a–d, which represent thick airfoil, the pressure here is dramatically increased up to maximum value at the leading edge (stagnation point) due to increasing flow velocity in the area of the leading edge on the suction surface where the velocity and AOA rises steeply (Kroo 2010). As shown in Fig. 6c, the pressure on the lower surface is always higher than the pressure on the upper surface. Furthermore, at the trailing edge, the flow on the upper surface decelerates and merges with the flow from the lower surface. Also, it is evident that the increased strength of the opposing pressure caused the forward movement of the separation point on the airfoil as well as the earlier separation of flow at higher AOA (Sørensen and Kock 1995).

The pressure distribution over four different airfoils S818, S827, S828 and FFA-W3-301 at different wind speeds and at different AOAs is demonstrated in Figs. 7, 8, 9 and 10. When the AOA is increased, the suction peak gradually builds up until AOA $= 16°$ (± 16). As a rule for higher angles of attack, the airfoil stalls and lift coefficient decreases.

According to Figs. 9e and 10e at $X/C = 0.3$, where the airfoil thickness is maximum, the pressure difference is large for S828 and FFA-W3-301. The process of pressure variation increase by the tip vane does not change. The effect of a pressure surface on the tip vane is small and on the suction surface is not yet large, especially at the blade tip. By shifting to trailing edge, the effect of pressure differences increases and the tip vane decreases. It is

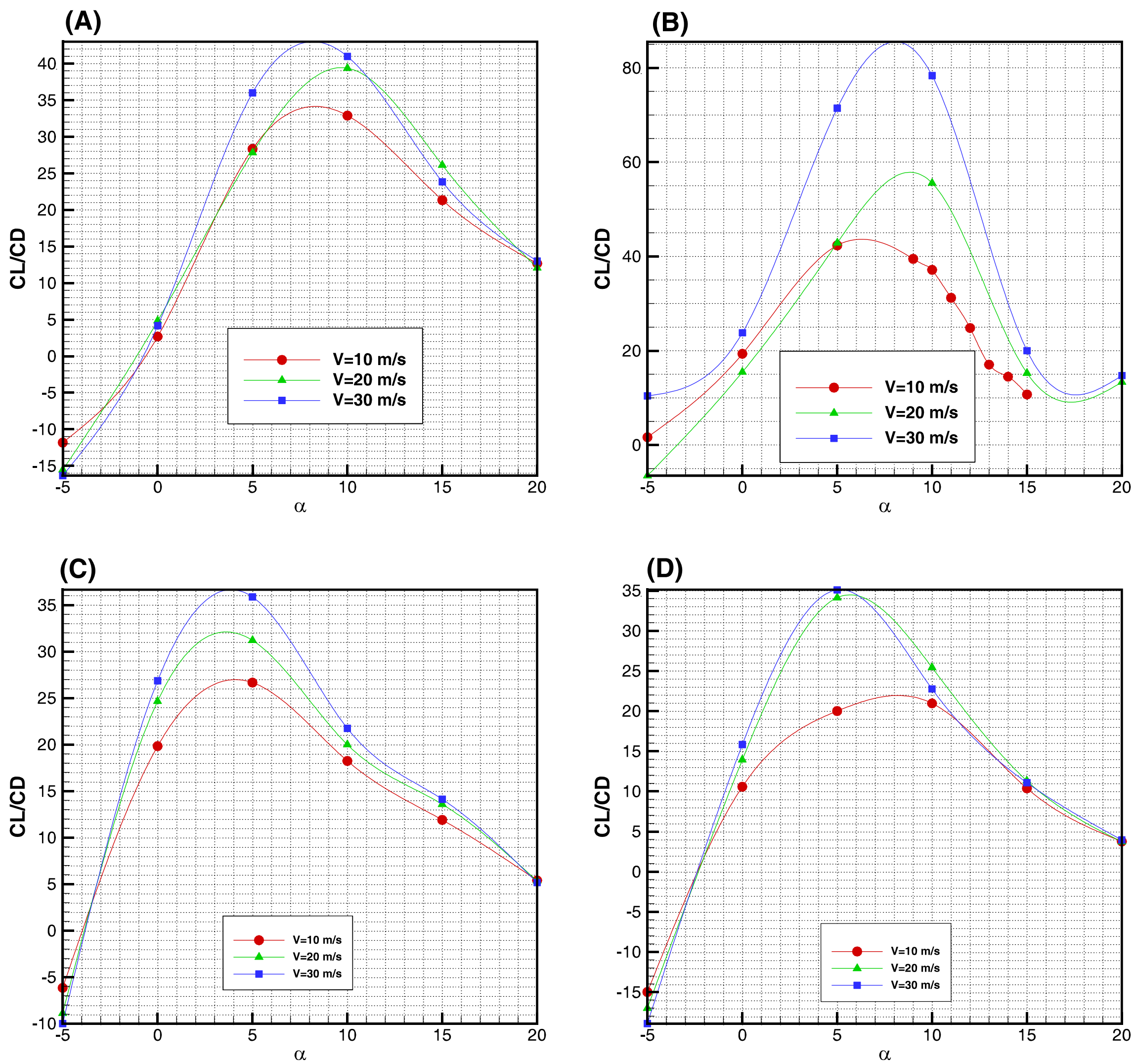

Fig. 5 Sliding ratio for some selected profiles at different wind speeds. **a** The sliding ratio for FFA-W3-301, **b** the sliding ratio for S818, **c** the sliding ratio for S827 and **d** the sliding ratio for S828

obvious that the greater effect by the tip vane and the greater pressure difference increase occur at the blade tip.

For this simulation, S818 and FFA-W3-301 were thick airfoils and other airfoils are thin because S818 and FFA-W3-301 are used in the root and others are primary tip ones. Figure 7f shows a C_p curve at $\alpha = 20°$ showing minimum and maximum values. The standard deviation was small on the pressure side and slightly increased at the suction side. The variation of the pressure distributions on pressure side has good results in the measurement in region close to the stagnation point. A closer look at Fig. 7f reveals that the CFD predictions show a leading edge separation for the $V = 30$ m/s at this section, whereas computations preserve a sharp suction peak. By comparison, lower surface area clearly shows that C_p curves are markedly declining before $X/C = 0.3$. However, for other models, this reduction in values occurs after $X/C = 0.3$, which is represented in Fig. 9f. As shown in Fig. 7d, the transition point occurs at $X/C = 0.3$. It was observed that the transition occurs when there is an increase in the pressure in the boundary layer, which is clearly shown in the pressure coefficient diagram. In the low-speed area, an adverse pressure gradient in the leading edge flow causes separation in laminar boundary layer and led to developing a free shear layer which for slightly higher-speed area. As a rule, when the boundary layer moves enough to an adverse pressure gradient, flow separation occurs, and therefore, speeds of the boundary layer dependent on the airfoil drop almost to zero. As expected, Figs. 7e and 9f show a fully attached flow at high angles of attack. Attached flow is the flow which has not been separated from the body. In an airfoil

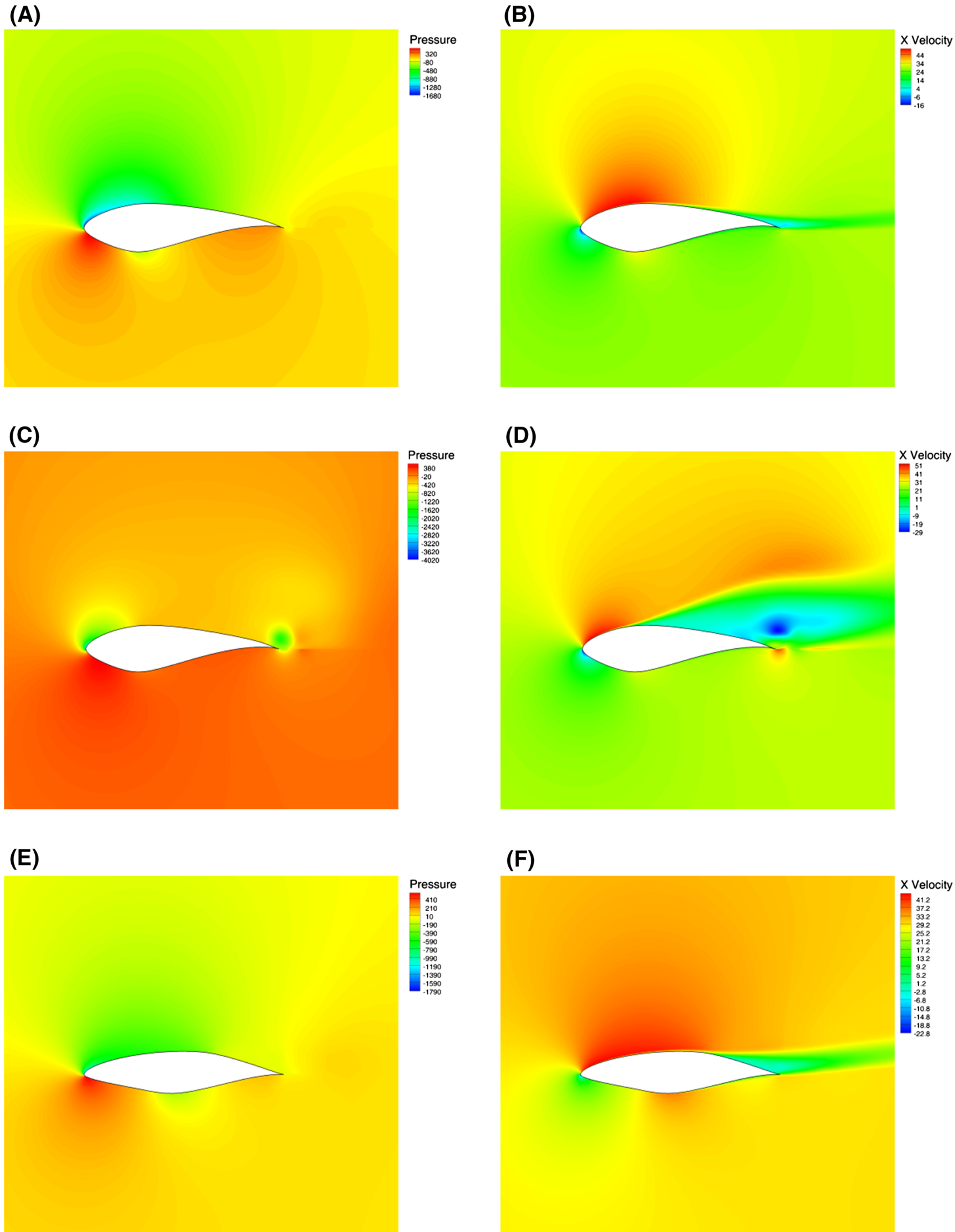

Fig. 6 Pressure and velocity contour. **a** pressure contour for S818, AOA = 10, $V = 30$, **b** velocity contour for S818, AOA = 10, $V = 30$, **c** pressure contour for S818, AOA = 20, $V = 30$, **d** velocity contour for S818, AOA = 20, $V = 30$, **e** pressure contour for S827, AOA = 10, $V = 30$, **f** velocity contour for S827, AOA = 10, $V = 30$, **g** pressure contour for S827, AOA = 20, $V = 30$, **h** velocity contour for S827, AOA = 20, $V = 30$, **i** pressure contour for S828, AOA = 10, $V = 30$, **j** pressure contour for S828, AOA = 10, $V = 30$, **k** pressure contour for S828, AOA = 20, $V = 30$ and **l** pressure contour for S828, AOA = 20, $V = 30$

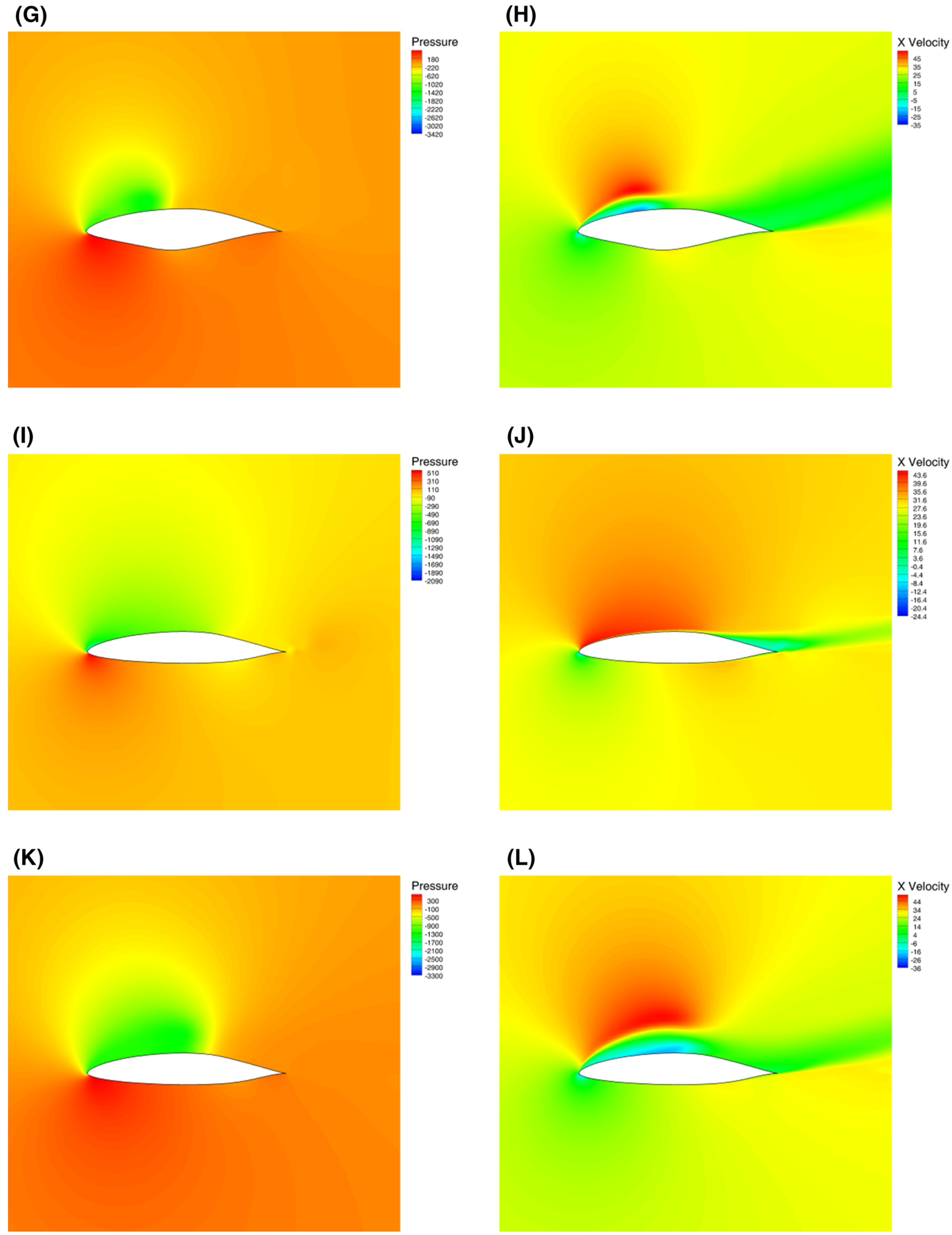

Fig. 6 continued

at low angles of attack, the flow is attached to surface. But when the AOA increases, the flow tends to "separate" as the fluid does not have enough momentum to stick to the surface. To obtain effect of fully turbulent flow, especially at these angles of attack, the calculations must apply an Euler calculation. This opinion is recommended by Wolfe (Walter et al. 1997) for S809 airfoils. The results are shown in Fig. 7b. The flow is separated on upper surface and lower surface at approximately $X/C = 0.3$, which is shown in Fig. 7d.

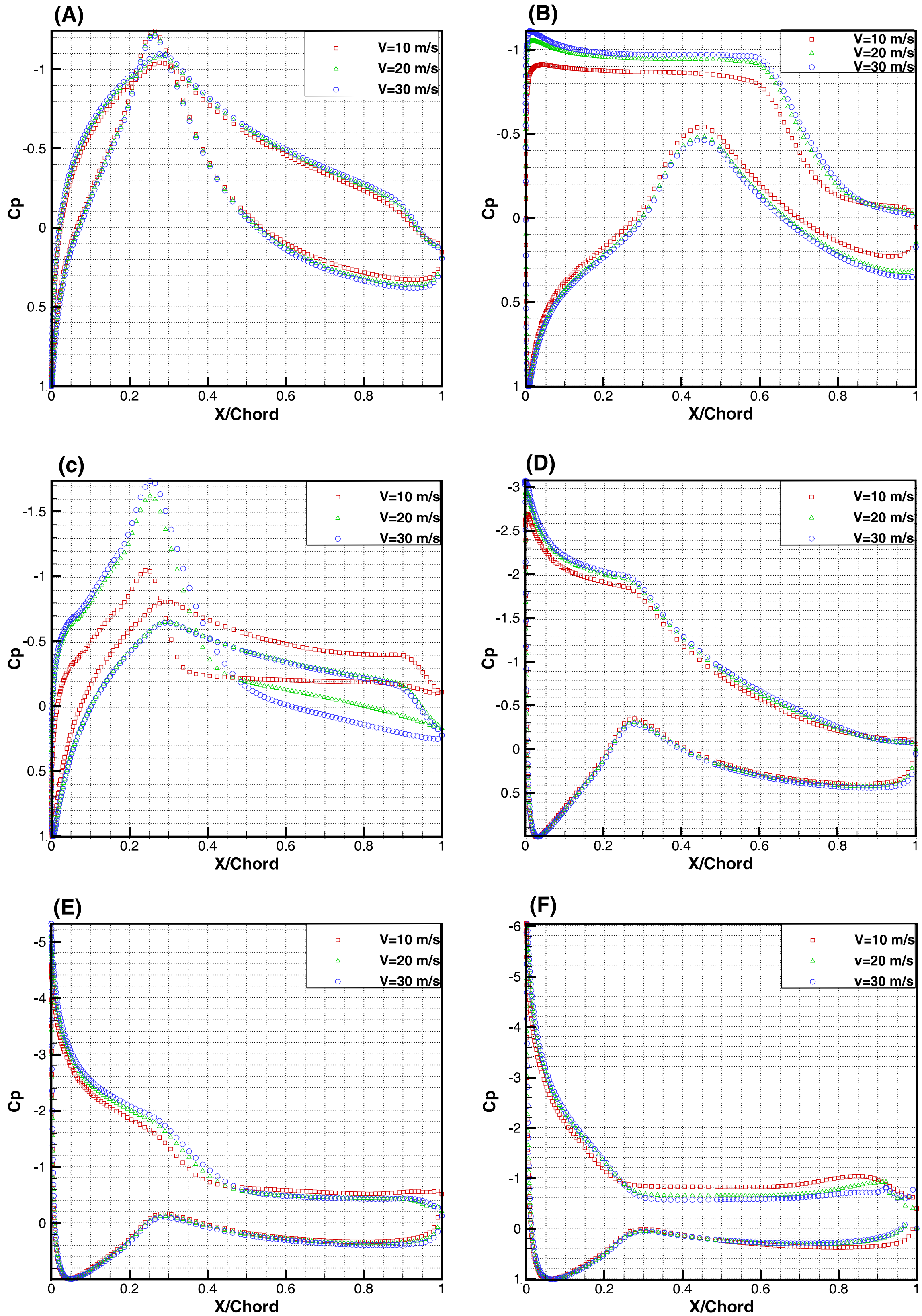

Fig. 7 S818 Pressure distributions. **a** $\alpha = 0°$, **b** $\alpha = 5°$, **c** $\alpha = -5°$, **d** $\alpha = 10°$, **e** $\alpha = 15°$ and **f** $\alpha = 20°$

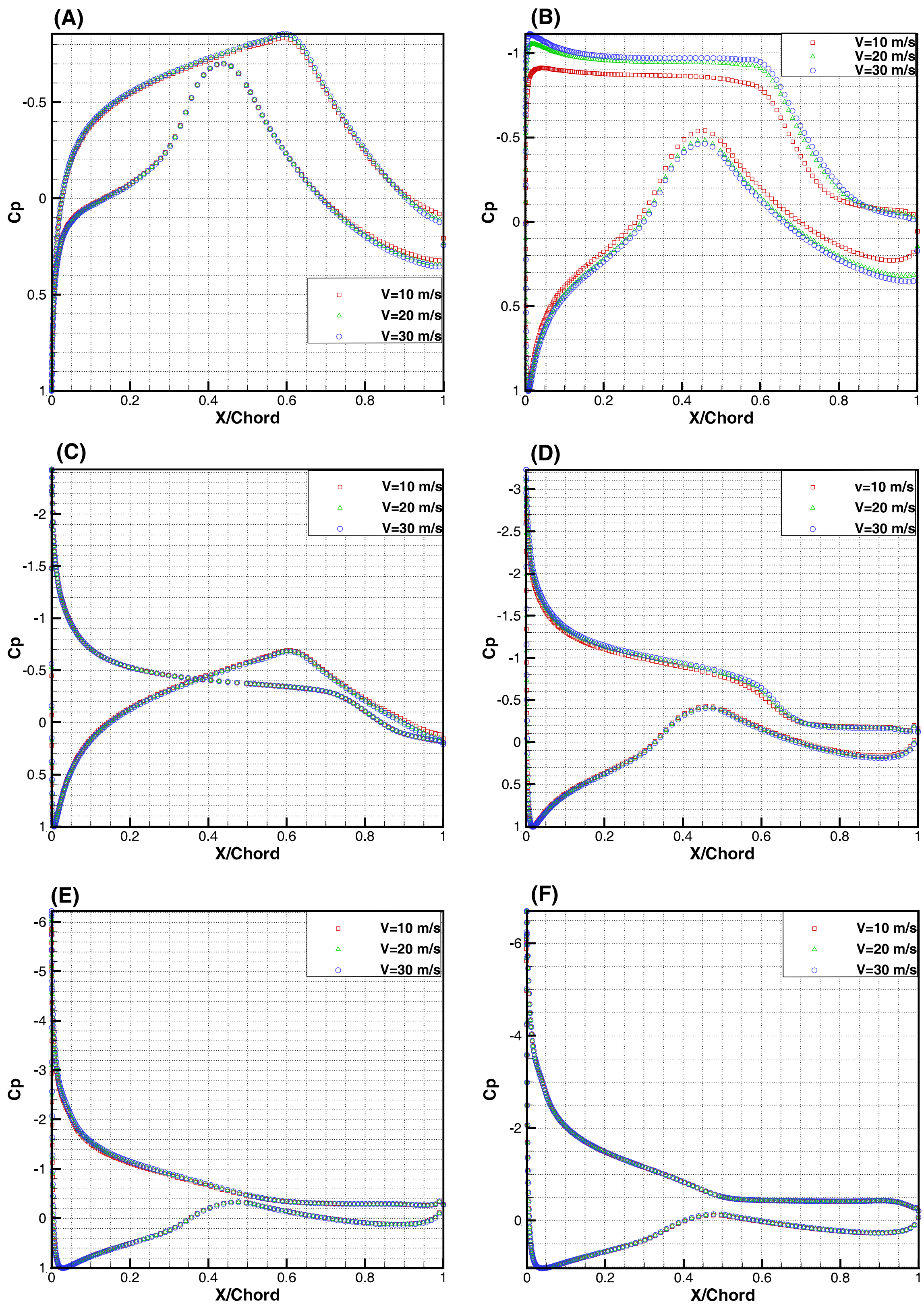

Fig. 8 S827 Pressure distributions. **a** $\alpha = 0°$, **b** $\alpha = 5°$, **c** $\alpha = -5°$, **d** $\alpha = 10°$, **e** $\alpha = 15°$ and **f** $\alpha = 20°$

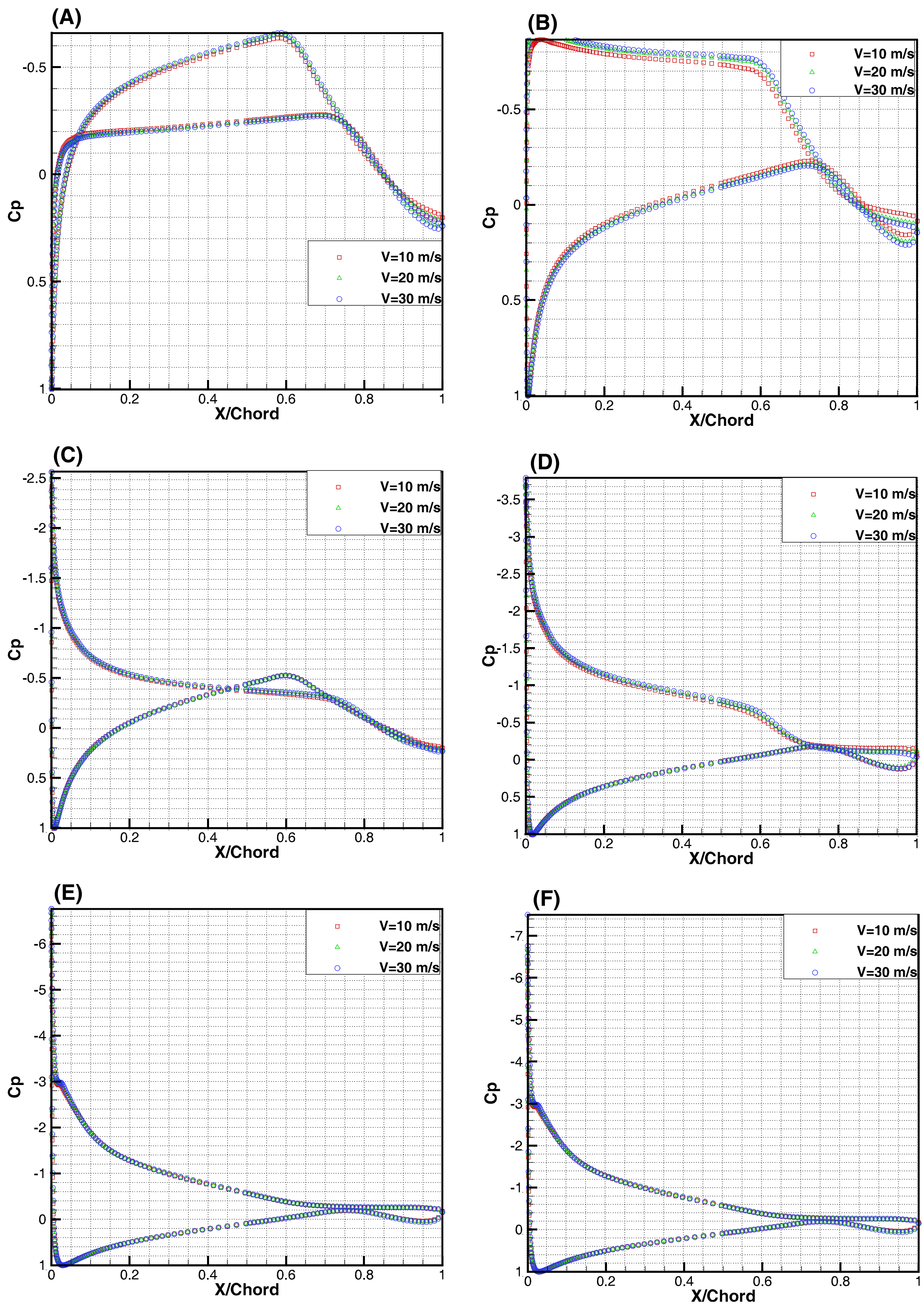

Fig. 9 S828 Pressure distributions. **a** $\alpha = 0°$, **b** $\alpha = 5°$, **c** $\alpha = -5°$, **d** $\alpha = 10°$, **e** $\alpha = 15°$ and **f** $\alpha = 20°$

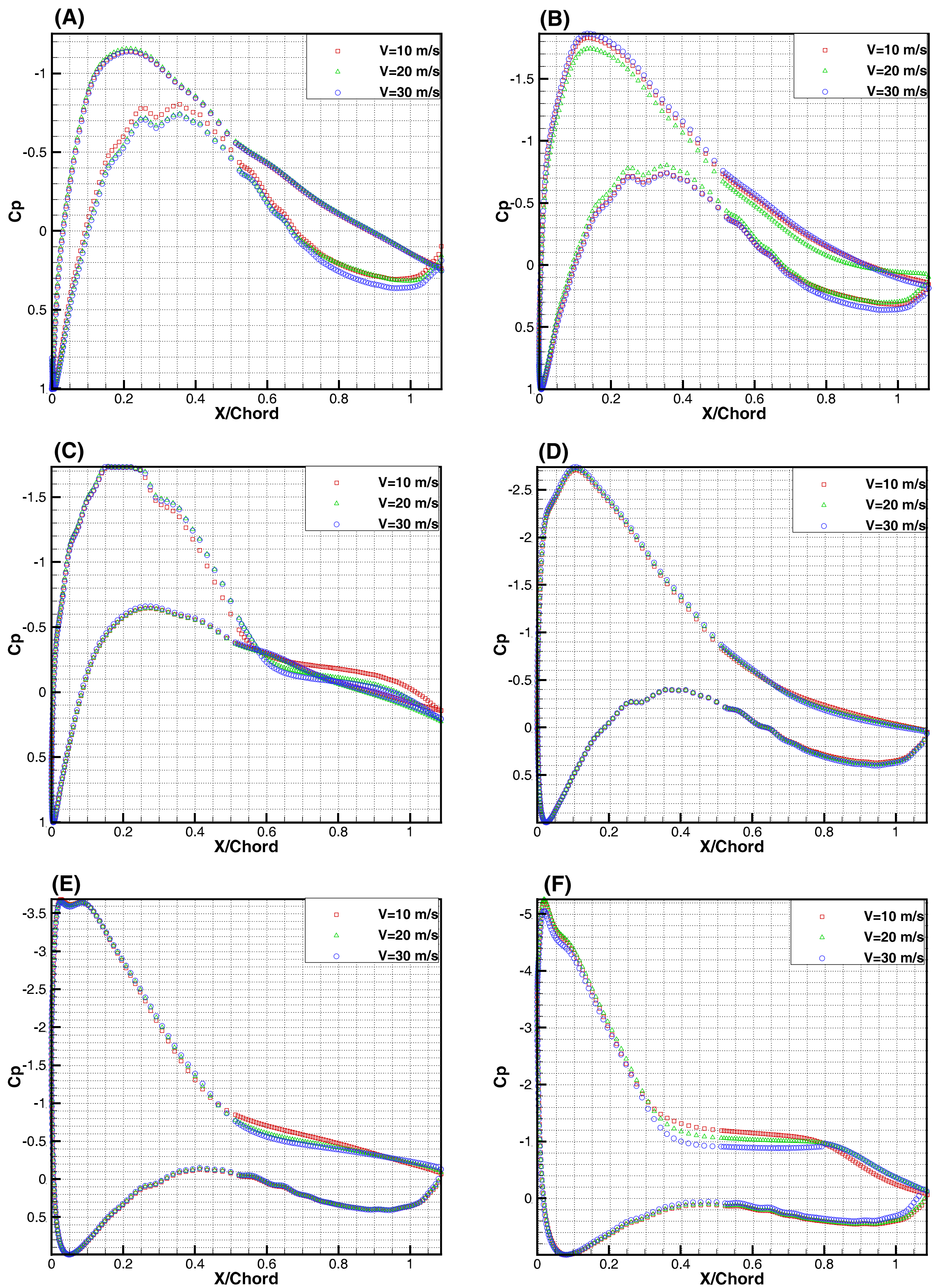

Fig. 10 FFA-W3-301 Pressure distributions. **a** $\alpha = 0°$, **b** $\alpha = 5°$, **c** $\alpha = -5°$, **d** $\alpha = 10°$, **e** $\alpha = 15°$ and **f** $\alpha = 20°$

S827 is similar to S809, especially on leading edge, because both of them have sharp leading edges. At low AOA ($\alpha = \pm 5°$), the lower surface stagnation point is displaced approximately behind the leading edge. In Fig. 10b, the transition location on upper and lower surface occurs at $X/C = 0.2$, approximately at the position of maximum thickness. For higher AOA Fig. 7f, the upper surface transition point changed position and moved forward to the leading edge in $X/C = 0.3$, and as shown in Fig. 8e, f, it occurred at $X/C = 0.4$. At $\alpha = 20°$, the flow is separated over upper surface after $X/C = 0.5$ (Fig. 8f).

Conclusion

The performance and the aerodynamic behavior of the S818, S827, S828, AH-94-W301 and FFA-W3-301 airfoils were investigated in this research. Results showed that an airfoil with high sliding ratio has higher efficiency. Meanwhile, it is deduced that the AOA does have a dominant effect on determining the optimum profile, while the wind speed does not. The optimum operating AOA should be between 0° and 10° for maximizing the sliding ratio and the power extracted from the wind. It is also noted that as the AOA increases above the optimum range, the sliding ratio decreases and the difference in the sliding ratios between all profiles becomes minimal. In this study, the pressure distribution and turbulence measurements were also taken at different velocities and AOAs on the airfoil section. Moreover, measurements of the pressure distribution in the flow field around the sections with different AOAs were studied. It should be noted that, as horizontal axis wind turbines routinely operate in the post-stall regime, accurate predications in this area are important. To understand where exactly post-stall was occurring and by considering that stall typically occurs at large angles of attack, depending on the airfoil design, the numerical results for unsteady flow were compared in the normal working range of operation; besides, attempts should be made to provide this concept in dynamic environment. The other important point is that where separation happens. In aerodynamics measurements, separation can make a significant contribution to increasing pressure drag over the upper surface and reducing lift, pressure drag which representing the pressure differential between the front and behind surfaces of the object. This condition is considered for wind turbines because it can be utilized to control the maximum power output to prevent unintentional generator overload and excessive forces in the blades during extreme wind speeds. The K–ω models are higher than K–ε ones because the K–ε models are not adequate for exact aerodynamic predictions at different AOAs in the post-stall region.

Acknowledgments The authors would like to extend their most sincere gratitude to the Sharif University of Technology for supporting the work by the Parallel Computing Laboratory Research (PCLR), which made a substantial contribution to this project.

List of symbols

Re	Reynolds number
C_D	Drag coefficient
C_p	Pressure coefficient
C_L	Lift coefficient
P	Local static pressure on the airfoil
p_∞	Free stream pressure
ρ	Air density
L	Lift force
D	Drag force
V	Velocity
υ	Kinematic viscosity
A	Area of the blade
α	Angle of attack
C	Airfoil chord
U	Wind speed
μ	Fluid viscosity
X	Length scale
τ_{ij}	Shear stress transport
μ_t	Turbulent eddy viscosity
δ_{ij}	Kronecker delta
σ_k	Turbulent diffusion coefficients
S_{ij}	Rate of strain tensor
υ_t	Turbulent kinematic viscosity
ω	Specific dissipation rate
Ω	Absolute value of the vorticity
K	Von Karman constant
γ	Coefficient in the production of dissipation
i, j, k	Indices

References

Ackermann T (2005) Wind power in power systems. Royal Institute of Technology, Stockholm

ANSYS (2014) ANSYS FLUENT user guide. ANSYS, USA, Nov 2014

Bjorck A (1990) Coordinates and calculations for the FFA-Wl-xxx, FFA-W2-xxx And FFA-W3-xxx series of airfoils for horizontal axis wind turbines. The Aeronautical Research Institute of Sweden, Aerodynamics Department FL Ygtekniska Forsoksanstalten, Stockholm

Björk A (1996) A guide to data files from wind tunnel test of A NACA 63-215 airfoil at FFA, Report FFAP-V-018

Borg M, Shires A, Collu M (2014) Offshore floating vertical axis wind turbines, dynamics modelling state of the art. Part I: Aerodynamics. Renew Sustain Energy Rev 39:1214–1225. doi:10.1016/j.rser.2014.07.096

Buhl M (2012) NREL airfoil families for HAWTs. National Laboratory of the U.S. Department of Energy (NREL), Golden

Cheng Z, Li R, Yang C, Hu W (2010) Criterion of aerodynamic performance of large-scale offshore horizontal axis wind turbines. Appl Math Mech 31(1):13–20. doi:10.1007/s10483-010-0102-2

Driss Z, Chelbi T, Kaffel A, Abid MS (2015) Experimental characterization of a NACA2415 airfoil wind turbine. In Haddar M, Abbes SM, Choley J-Y, Boukharouba T, Elnady T, Kanaev A, Ben Amar M, Chaari F (eds) Multiphysics modelling and simulation for systems design and monitoring: proceedings of the multiphysics modelling and simulation for systems design conference, MMSSD 2014, 17–19 Dec, Sousse, Tunisia, pp 111–120. Springer, Cham

Farrugia R, Sant T, Micallef D (2014) Investigating the aerodynamic performance of a model offshore floating wind turbine. Renew Energy 70:24–30. doi:10.1016/j.renene.2013.12.043

Fuglsang P, Bak C (2004) Development of the Risø wind turbine airfoils. Wind Energy 7(2):145–162. doi:10.1002/we.117

Gatski TB, Bonnet J-P (2009) Compressibility, turbulence and high speed flow. Elsevier, Amsterdam

Gonzalez A, Munduate X (2007). Three dimensional and rotational aerodynamics on the NREL phase VI wind turbine blade. Paper presented at the 45th AIAA aerospace sciences meeting and exhibit, Reno, NV, Jan 2009

Gudmundsson S (2014) Chapter 8: The anatomy of the airfoil. General aviation aircraft design. Butterworth-Heinemann, Boston, pp 235–297

Hansen AC, Butterfield CP (1993) Aerodynamics of horizontal-axis wind turbines. Annu Rev Fluid Mech 25(1):115–149

Hirsch C (1990) Numerical computation of internal and external flows, vol 2. Wiley, London

Karbasian HR, Esfahani JA, Barati E (2014) Effect of acceleration on dynamic stall of airfoil in unsteady operating conditions. Wind Energy. doi:10.1002/we.1818

Kim B, Kim W, Bae S, Park J, Kim M (2011) Aerodynamic design and performance analysis of multi-MW class wind turbine blade. J Mech Sci Technol 25(8):1995–2002. doi:10.1007/s12206-011-0521-x

Kroo I (2010) Aircraft design: synthesis and analysis. Stanford University, Stanford

Langtry RB, Gola J, Menter FR (2006) Predicting 2D airfoil and 3D wind turbine rotor performance using a transition model for general CFD codes. Paper presented at the 44th AIAA aerospace sciences meeting and exhibit, Reno, NV, Jan 2006

Liu Y, Yang C, Song X (2015) An airfoil parameterization method for the representation and optimization of wind turbine special airfoil. J Therm Sci 24(2):99–108. doi:10.1007/s11630-015-0761-7

Ma D, Zhao Y, Qiao Y, Li G (2015) Effects of relative thickness on aerodynamic characteristics of airfoil at a low Reynolds number. Chin J Aeronaut 28(4):1003–1015. doi:10.1016/j.cja.2015.05.012

Manwell J (2012) Offshore wind energy offshore wind energy technology trends, challenges, and risks. In: Meyers R (ed) Encyclopedia of sustainability science and technology. Springer, New York, pp 7393–7425

Manwell JF, McGowan JG, Rogers AL (2009) Aerodynamics of wind turbines wind energy explained. Wiley, pp 91–155

Mark P, Dimitri M (2009) Unstructured mesh CFD aerodynamic analysis of the NREL phase VI rotor. In: 47th AIAA aerospace sciences meeting including the new horizons forum and aerospace exposition. American Institute of Aeronautics and Astronautics, Orlando, FL

Menter FR (1994) Two-equation eddy-viscosity turbulence models for engineering applications. AIAA J 32(8):1598–1605

Radmanesh AR, Abbaspour M, Soltani MR (2014) Unsteady aerodynamic analysis of different multi MW horizontal axis wind turbine blade profiles on SST-K-ω model. Paper presented at the 7th international exergy, energy and environment symposium (IEEES-7), Valenciennes, France

Radmanesh AR, Abbaspour M, Soltani MR (2015a) Numerical simulation of unsteady flow of the effects of pressure distribution of different multi MW horizontal axis wind turbine blade profiles on SST-K-ω model. Paper presented at the ISME2015, Tehran, Iran

Radmanesh AR, Abbaspour M, Soltani MR (2015b) Unsteady aerodynamic analysis of different multi MW horizontal axis offshore wind turbine blade profiles on SST-K-ω model. Paper presented at the ISME2015, Tehran, Iran

Sayed MA, Morgan KH (2011) Computational fluid dynamics study of wind turbine blade profiles at low Reynolds' number for various angles of attack. Paper presented at the 4th international meeting on advances in thermofluids, Melaka, Malaysia

Sayed MA, Kandil HA, Shaltot A (2012) Aerodynamic analysis of different wind-turbine-blade profiles using finite-volume method. Energy Convers Manag 64:541–550. doi:10.1016/j.enconman.2012.05.030

Slooff JW (2015) Elements of fluid mechanics (air and water). In: S. I. Publishing (ed) The aero- and hydromechanics of keel yachts. Springer, Berlin

Somers DM (2005) The S827 and S828 airfoils. In: P. u. S. N. AAF-4-14289-01 (ed) NREL/SR-500-36343. Airfoils, Inc. State College, Pennsylvania and National Renewable Energy Laboratory Proprietary to NREL

Sørensen JN, Kock CW (1995) A model for unsteady rotor aerodynamics. J Wind Eng Ind Aerodyn 58(3):259–275. doi:10.1016/0167-6105(95)00027-5

Tangler JL (1982) Comparison of wind turbine performance prediction and measurement. J Sol Energy Eng 104(2):84–88. doi:10.1115/1.3266290

van Rooij RPJOM, Timmer WA (2003) Roughness sensitivity considerations for thick rotor blade airfoils. J Sol Energy Eng 125(4):468–478. doi:10.1115/1.1624614

Walter W, Stuart O, Walter W, Stuart O (1997) CFD calculations of S809 aerodynamic characteristics. In: 35th aerospace sciences meeting and exhibit. American Institute of Aeronautics and Astronautics

Wilcox DC (2006) Turbulence modeling for CFD. DCW Industries, CA

Yelmule MM, EswaraRao Anjuri VSJ (2013) CFD predictions of NREL phase VI rotor experiments in NASA/AMES wind tunnel. Int J Renew Energy Res 3(2)